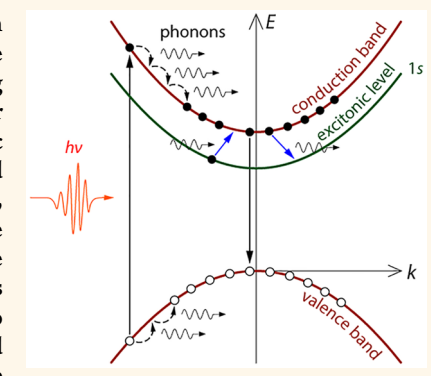
Monitoring Electron-Phonon Interactions in Lead Halide Perovskites Using Time-Resolved THz Spectroscopy

Daming Zhao,† Hongwei Hu,‡ Reinhard Haselsberger,† Rudolph A. Marcus,†,§ Maria-Elisabeth Michel-Beyerle,[†] Yeng Ming Lam,[‡] Jian-Xin Zhu,[†] Chan La-o-vorakiat,*,^{||, \triangle} Matthew C. Beard,*, and Elbert E. M. Chia*, to

Supporting Information

Downloaded via CALIFORNIA INST OF TECHNOLOGY on December 6, 2019 at 22:31:11 (UTC). See https://pubs.acs.org/sharingguidelines for options on how to legitimately share published articles.

ABSTRACT: Lead halide perovskite semiconductors have low-frequency phonon modes within the lead halide sublattice and thus are considered to be soft. The soft lattice is considered to be important in defining their interesting optoelectronic properties. Electron-phonon coupling governs hot-carrier relaxation, carrier mobilities, carrier lifetimes, among other important electronic characteristics. Directly observing the interplay between free charge carriers and phonons can provide details on how phonons impact these properties (e.g., exciton populations and other collective modes). Here, we observe a delicate interplay among carriers, phonons, and excitons in mixed-cation and mixed-halide perovskite films by simultaneously resolving the contribution of charge carriers and phonons in time-resolved terahertz photoconductivity spectra. We are able to observe directly the increase in phonon population during carrier cooling and discuss how thermal equilibrium populations of carriers and phonons modulate



the carrier transport properties, as well as reduce the population of carriers within band tails. We are also able to observe directly the formation of free charge carriers when excitons interact with phonons and dissociate and to describe how free carriers and exciton populations exchange through phonon interactions. Finally, we also time-resolve how the carriers are screened via the Coulomb interaction at low and room temperatures. Our studies shed light on how charge carriers interact with the low-energy phonons and discuss implications.

KEYWORDS: perovskite, time-resolved terahertz spectroscopy, phonon, free carrier, exciton

he combination of excellent photovoltaic performance and solution processability has brought organicinorganic hybrid perovskites into the forefront of solar cell research. The collusion of favorable properties, such as strong and broad-band visible light absorption² and long $(\sim 1 \mu m)$ and balanced electron and hole diffusion lengths,^{3,4} ensures that, upon solar illumination, electron-hole pairs can form, dissociate, and quickly drift away from the active regions

and toward the electrodes before loss processes such as recombination occur.

The most studied lead halide perovskite is methylammonium lead iodide (MAPbI₃).⁴⁻⁷ However, MAPbI₃ suffers from stability issues, such as degradation by ultraviolet light

Received: March 15, 2019 Accepted: July 26, 2019 Published: July 26, 2019

[†]Division of Physics and Applied Physics, School of Physical and Mathematical Sciences, Nanyang Technological University, 637371 Singapore

^{*}School of Materials Science and Engineering, Nanyang Technological University, 639798 Singapore

[§]Noyes Laboratory, California Institute of Technology, Pasadena, California 91125, United States

¹Theoretical Division and Center for Integrated Nanotechnologies, Los Alamos National Laboratory, Los Alamos, New Mexico 87545, United States

Nanoscience and Nanotechnology Graduate Program, Faculty of Science, King Mongkut's University of Technology Thonburi (KMUTT), Bangkok 10140, Thailand

[△]Theoretical and Computational Science Center (TaCS), KMUTT, Bangkok 10140, Thailand

[¶]Chemistry and Nanoscience Science Center, National Renewable Energy Laboratory, Golden, Colorado 80401, United States

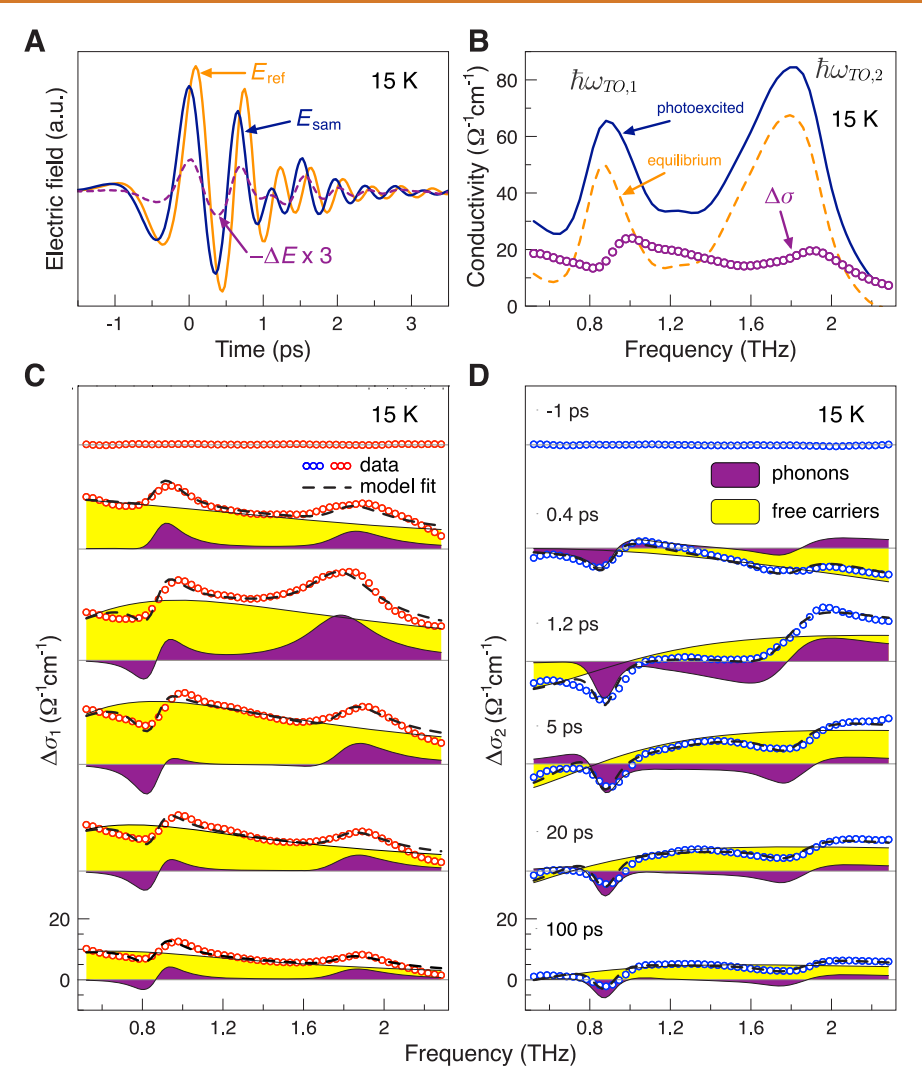


Figure 1. Frequency-resolved photoconductivity spectra. (A) THz time-domain data of the alloyed FA perovskite $FA_{0.85}Cs_{0.15}Pb(I_{0.97}Br_{0.03})_3$ thin films after optical excitation with 790 nm pump pulses. The photoconductivity is calculated from the transmitted THz electric field through the perovskite film (E_{sam}) , z-cut quartz reference (E_{ref}) , and the photoinduced change (ΔE) . (B) Real part of photoconductivity $[\Delta\sigma_1(\omega)]$ (purple circles) obtained by the difference between the photoexcited (navy blue) and the equilibrium THz conductivity (orange). The two peaks show the approximate locations of the lowest-lying TO phonon modes. The (C) real and (D) imaginary part of THz photoconductivity at different pump-probe delays, showing the contributions from Drude-Smith (DS, yellow area) and peak-shift (PS, purple area) terms. The DS term arises from photogenerated charge carriers in a disordered background, whereas the PS term accounts for the change in the oscillator strength and phonon resonant frequency.

and moisture in air. ^{8,9} By mixing the inorganic cesium cation in both MAPbX₃ (X = Cl, Br, or I) and $HC(NH_2)_2PbX_3$ (FAPbX₃), the stability can be greatly improved. ^{10,11} In addition, the band gap becomes tunable from 1.73 to 1.48 eV by increasing the size of the cation from Cs to MA to FA and from 1.48 to 2.23 eV by mixing bromine and iodine halides. ¹² One of the highest power conversion efficiencies (PCEs) of 22.1% ¹³ is obtained from solar cells based on mixed-cation and mixed-halide systems. We therefore focus our study on these mixed-cation and mixed-halide systems rather than the canonical MAPbI₃.

In our work, we capture both free-carrier and low-frequency phonon dynamics by utilizing a broad-band terahertz (THz) probe pulse. In the THz frequency range (1 THz = 4.1 meV), free carriers readily absorb the THz light with an absorption cross section that is proportional to the carrier mobility through a Drude-type mechanism. Within the same THz frequency range are the resonance frequencies of the lowest-

lying optical phonon modes. These phonon modes originate from vibrations of the metal halide sublattice. $^{15-17}$ In fact, one of the features of Pb halide perovskites that distinguishes them from traditional semiconductors is that optical phonon modes are low in energy, indicating a soft lattice with easily polarizable bonds. Here, we take advantage of the spectral overlap of energies to study the carrier population number and the phonon dynamics simultaneously, giving great insight into carrier-phonon interactions. That is, time-resolved THz spectroscopy (TRTS) is able to monitor the photoinduced carrier dynamics and carrier-induced changes in phonon modes simultaneously. Moreover, frequency-resolved TRTS extracts both the real and imaginary parts of the photoinduced change in the complex optical conductivity (or photoconductivity), without the need to invoke Kramers-Kronig transformation. Knowledge of both the real and imaginary parts of the dielectric function restricts the physical models

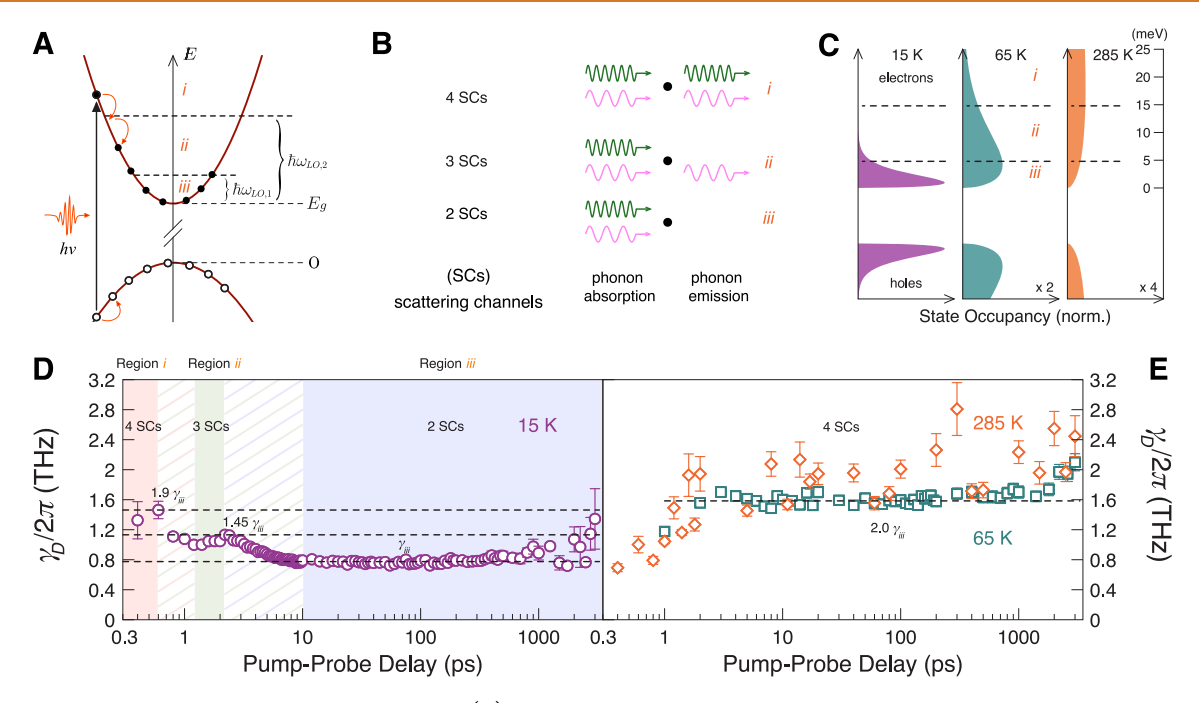


Figure 2. Energy-dependent carrier relaxation channels. (A) Optical excitation generates free electrons that relax from region i down toward iii delineated by phonon mode energies $\hbar\omega_{\text{LO},1}$ and $\hbar\omega_{\text{LO},2}$. Only electrons with kinetic energy above the phonon mode energy can both absorb and emit a phonon; only phonon absorption can occur with lower kinetic energy. (B) Number of electron scattering channels decreases from 4 to 3 to 2 as the electrons relax from regions i to ii to ii to ii. (C) Finite-temperature state occupancy calculated from the Fermi–Dirac distribution and density of states in a three-dimensional parabolic band, showing a temperature-dependent high-energy tail. State occupancies are normalized by the total carrier density. (D) Step-like transitions of carrier scattering rate (three horizontal dashed lines), obtained from the Drude–Smith model, in the ratio of 3.8:2.9:2.0. This is close to the 4:3:2 ratio deduced from the number of scattering channels as the electrons relax toward the band edge going from region i to ii to ii. The larger error bars at very long time delays may be due to the small photoinduced signals. (E) With sufficient thermal energy at 65 and 285 K, there is a significant fraction of carriers in region i (see Figure 2C), opening up all four scattering channels. This results in the scattering rate at 65 K scaling closer to a factor of 4/2 and a slightly higher value at 285 K.

that can explain the data, which is crucial for subsequent data interpretation.

Previous studies have shown that the frequency-resolved TRTS data exhibit features near the phonon mode frequencies. However, care must be taken to avoid data analysis artifacts. ¹⁸ Moreover, those studies attributed these features to carrier—phonon coupling without a suitable model ^{19,20} that can adequately describe their data. Furthermore, those studies only focus on carrier recombination and track only the long-time dynamics after ~5 ps, missing out on earlier time dynamics such as carrier cooling.

For the mixed-cation mixed-halide perovskite films studied in this paper, our analysis of dynamics from 0.4 to 3000 ps, at both low and room temperatures, reveals a significant change in the phonon mode profile and carrier-phonon scattering channels during carrier relaxation (earlier than 10 ps). Analysis of the carrier and phonon spectral weights reveals correlations between them that suggest the intricate interplay among phonon emission during carrier relaxation, exciton dissociation via phonon absorption, and photoenhanced carrier screening that cooperatively ensures a large and long-lived carrier population. Though one can observe carrier relaxation from transient absorption spectroscopy^{21,22} or deduce carrierphonon coupling from photoluminescence measurements,²³ in our experiments, we are able to, within the same set of data, explain the dynamics of carriers, excitons, and phonons and their mutual interplay, all within one self-consistent picture.

RESULTS AND DISCUSSION

Extraction of Phonon and Carrier Contribution. We begin our investigation of $FA_{0.85}Cs_{0.15}Pb(I_{0.97}Br_{0.03})_3$ thin film (FCPIB) by measuring the equilibrium (i.e., without pump, or dark) complex optical conductivity $\tilde{\sigma}(\omega) = \sigma_1(\omega) + i\sigma_2(\omega)$ at 15 K, as shown in Figure 1B. We observe peaks at 0.85 THz ($\hbar\omega_{TO,1}=3.6$ meV) and 1.80 THz ($\hbar\omega_{TO,2}=7.4$ meV) that originate from transverse-optical (TO) phonon absorption (labeled as modes 1 and 2, respectively). They correspond to a series of TO phonon modes related to the vibrations of Pb halide bonds. Their conductivity can be described by a Lorentzian profile. We performed a loss function analysis 17,25,26 (Supporting Information Figure S1B) and found the longitudinal-optical (LO) phonon modes to be located at higher energies of 1.15 THz ($\hbar\omega_{LO,1}=4.8$ meV) and 3.57 THz ($\hbar\omega_{LO,2}=14.8$ meV).

Next, we excite FCPIB with 60 fs, $37 \, \mu \text{J/cm}^2$ laser pulses with a photon energy of 1.57 ± 0.02 eV. In this work, all TRTS measurements were performed under the same excitation conditions. The photon energy is close to the band gap energy of ~ 1.57 eV (Supporting Information Figure S4), which has just enough energy to create excitons and electron—hole plasma with very little excess energy and avoids complex scenarios such as hot-carrier injection or multiple valley excitations. We then vary the optical path difference to scan the time delay τ between the optical pump pulse and THz probe pulse to obtain a full two-dimensional frequency-resolved THz

spectra of FCPIB photoconductivities (Figure 1C,D) (see Methods section).

Our frequency-resolved photoconductivities do not display only a Drude-like characteristic as is expected for photogenerated free charge carriers, but rather they also contain a derivative-like profile located near the two phonon peaks determined from our dark measurements. Such features have been reported on other perovskite semiconductors, either as a dip in the transmission spectra of MAPbI_{3-x}Cl_x¹⁹ or as an asymmetric photoinduced phonon profile in the photoconductivity spectra of MAPbI₃. These features were attributed to the presence of carrier—phonon coupling, though the asymmetry seen here in FCPIB is more pronounced. The photoconductivity can be quantitatively described by a combination of Drude–Smith (DS) and peak-shift (PS) contributions (see Supporting Information, section S10, for more details):

$$\Delta \widetilde{\sigma}(\omega, \tau) = \Delta \widetilde{\sigma}_{DS} + \Delta \widetilde{\sigma}_{PS}$$

where the DS term is conventionally used to account for the presence of free charge carriers inside a disordered environment. The probability of the DS contribution to the overall response, we can determine the carrier density and the carrier scattering rate. We introduce the PS term that accounts for a change in the phonon profile in the presence of free carriers. Both the resonant frequency and oscillator strength of the phonon modes are modified, and the PS term has a mathematical form that is related to the derivative of the Lorentzian function. We attribute this change in the phonon profile to the combined effects of phonon anharmonicity (predicted by density functional theory in MAPbI₃)²⁹ and large ionic displacements upon photoexcitation (from ultrafast electron diffraction data)⁷ (see Supporting Information, section S8, for more discussions).

From using a nonlinear least-squares fitting routine to find best-fit parameters that describe our observed data, we extract the photogenerated free charge carrier density (*via* the Drude plasma frequency), carrier scattering rate (*via* the Drude scattering rate), and the modulation of phonon profiles (*via* the PS terms).

Carrier-Phonon Scattering Channels: Physical Model and Experimental Data. Before we discuss the best-fit parameters, we first introduce the carrier relaxation scheme that we deduced from our data (Figure 2A,B).³⁰ For simplification, we only describe the relaxation from the perspective of electrons, as holes are expected to behave similarly due to their roughly equal effective masses.³¹

Immediately after photoexcitation, electrons thermalize within 100 fs. 21,22 Electrons possess energies (in excess of the band gap) above the two lowest-lying LO phonon modes. Carrier relaxation is dominated by carrier—LO phonon interactions via the Fröhlich mechanism. The energies of the two LO phonon modes motivate us to partition the electron relaxation process into three regions i, ii, iii, as shown in Figure 2A. In region i, where the electron energy E is larger than that of the two LO phonon modes $(E > \hbar \omega_{\text{LO},1})$, electrons can interact with the two phonon modes via four scattering channels—phonon absorption and emission from both modes 1 and 2.

The electrons then lose energy and enter region ii, where $\hbar\omega_{\text{LO},2} > E > \hbar\omega_{\text{LO},1}$. Here, the electrons do not have enough energy to participate in the carrier—phonon scattering process that involves the emission of $\hbar\omega_{\text{LO},2}$ phonons, so there are now

only three energetically permissible scattering channels. Similarly, as the electrons relax close to the conduction band minimum in region iii ($\hbar\omega_{\text{LO},2} > \hbar\omega_{\text{LO},1} > E$), they cannot emit either $\hbar\omega_{\text{LO},1}$ or $\hbar\omega_{\text{LO},2}$ phonons, and we are left with only two scattering channels of phonon absorption. At the bottom of the band, carrier recombination across the band gap dominates.

The above picture is strictly valid at 0 K. At finite temperatures, thermal broadening caused by the high-energy tail in the Fermi-Dirac distribution and hence state occupancy distribution (see Figure 2C) results in transitions between the regions to be gradual rather than step-like. For example, inside region ii, even though the mean energy $\langle E \rangle$ of the electrons obeys $\hbar\omega_{\rm LO,2} > \langle E \rangle > \hbar\omega_{\rm LO,1}$, a small fraction of the electrons can still be located in region i, which opens up all four scattering channels there. At room temperature, all four scattering channels open up at all time delays, enabling electron relaxation to take place simultaneously with carrier recombination. Thus, a thermal distribution of electrons, phonons, and excitons are produced. Carriers interact strongly with phonons by continually losing and gaining energy to maintain the thermal distribution at room temperature. This is quite distinct from other typical semiconductors with larger LO phonon mode energies than in the halide perovskites, where thermalized carriers cannot emit phonons, and the phonon population at room temperature is not so great such that carriers do not continually interact with a large population of phonons. In our system, the carriers are constantly emitting and absorbing phonons. Two main consequences arise from these interactions: (1) it limits the carrier mobility as the number of scattering channels is increased, and (2) it provides a pathway to detrap carriers from shallow band tails.

The experimental evidence of quasi-step-like reduction of scattering channels and our regional assignment of the conduction band are found in the measured carrier scattering rate extracted through Drude analysis (Figure 2D,E), which is proportional to the number of scattering channels according to Matthiessen's rule.³² At the low temperature of 15 K, where there is minimal thermal broadening, Figure 2D shows that the scattering rates at early (region i: τ < 0.6 ps), intermediate (region ii: 1.2 ps $< \tau < 2.2$ ps), and long (region iii: $\tau > 10$ ps) time delays exist in the approximate ratio of 3.8:2.9:2.0. This is close to the 4:3:2 ratio expected from the number of possible scattering channels in the three regions. Additional support for our interpretation is provided by data at higher temperatures (65 K \approx 5.4 meV and 285 K \approx 24 meV); see Figure 2E. Due to thermal broadening at finite temperatures (see Figure 2C), electrons can now populate region i (with four scattering channels) with finite probability, with two consequences: (1) the 65 and 285 K scattering rates are similar to that of the 15 K data with four scattering channels, and (2) the change of scattering rate between regions is no longer observable. The fact that the four-channel scattering rate at 285 K is slightly higher than that at 65 K, which in turn is slightly larger than that at 15 K, is again a consequence of a longer Fermi-Dirac high-energy tail with increasing temperature.

It is interesting to note that the scattering rate at early times $(\tau \leq 1 \text{ ps})$ for 65 and 285 K is smaller than the long-delay-time values, that is, showing fewer than four scattering channels. As we are exciting our sample with 20 meV bandwidth photons centered at the band edge ($\sim 1.57 \text{ eV}$), a majority of the photoexcited carriers would have a kinetic energy of only 5–10 meV, that is, $\sim 60-120 \text{ K}$. Thus, after about 100 fs, the thermalized carriers would have a lower temperature than the

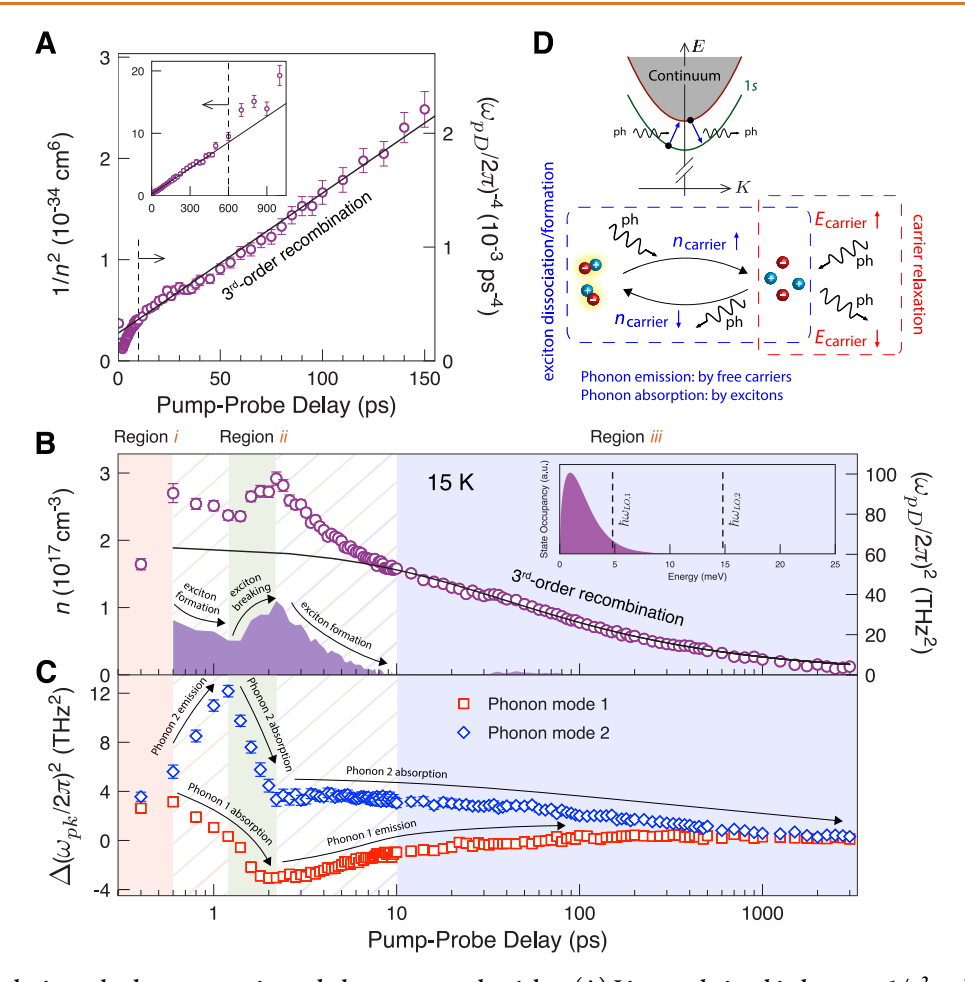


Figure 3. Resolving the interplay between carrier and phonon spectral weights. (A) Linear relationship between $1/n^2$ and pump—probe delay τ indicates predominantly third-order recombination, especially in the region between 10 and 600 ps. The deviation of the data from linearity below 10 ps suggests that carrier recombination is dominant after 10 ps, *i.e.*, in region iii near the band edge (see Figure 2A). (B) Time evolution of the photogenerated carrier density n at 15 K. Solid line is the third-order recombination curve plotted using the weighted-least-squares linear-fit parameters (between 10 and 600 ps) in (A) then extrapolated down to 0.6 ps and up to 3000 ps. The difference between the experimental data and solid curve is indicated by the purple region. (C) Time evolution of the photoinduced change in spectral weight of phonon mode 1 (0.85 THz) and mode 2 (1.80 THz). By comparing panels (B) and (C), one sees that, in region ii, a decrease in the spectral weight of both phonon modes is accompanied by an increase in carrier density. This can happen only when phonons are absorbed by the excitons, thereby dissociating the excitons to become free carriers. In region iii, where the carriers are already near the band edge, phonon emission and absorption slow down, and (third-order) recombination is now dominant. (D) Schematic showing phonon-related mechanisms that affect carrier density and carrier energy. Top figure depicts the excitation spectrum of electron—hole pairs with energy E and center-of-mass momentum E and the processes of exciton dissociation (formation) accompanied by phonon absorption (emission) by excitons (free carriers). Only the 1s excitonic level is shown for clarity.

lattice at higher temperatures (e.g., 65 and 285 K) and so would not have access to all four scattering channels. Subsequently, these carriers are then "warmed up" by the lattice after a few hundred femtoseconds.

Note that scattering from acoustic phonons is significant only when the carriers have cooled to near the band edge, such that the carrier energy is smaller than the energy of both LO phonon modes, that is, region *iii* in our analysis. In regions *i* and *ii*, the carrier relaxation time is dominated by interactions with LO phonons through the Fröhlich interaction. Hence, in our present work on a halide perovskite semiconductor, it is reasonable to consider only the carrier—LO phonon interaction in our analysis and interpretation.

Here, we are able to resolve directly the subtle role that phonons play in thermalized carrier distribution. The energies of the lowest-lying phonon modes, relative to the operation temperature, determine the number of carrier scattering channels and hence the scattering rate and carrier mobility of photogenerated free carriers. The carrier relaxation dynamics picture obtained in this section forms the basis of our subsequent analysis of carrier density and phonon spectral weights, which will be discussed in the following sections.

Disentanglement of Carrier Recombination and Relaxation. Next, we show that the phonons, *via* their emission by free carriers and/or absorption by excitons, directly affect the density of photogenerated carriers. We do this by monitoring two types of spectral weights: (1) Drude spectral weight, which is proportional to the square of the Drude plasma frequency $(\omega_{\rm pD}^2)$, is a direct measure of the number density of photogenerated free charge carriers, $n = \epsilon_0 \omega_{\rm pD}^2 m^{**}/e^2$, where $m^{**} = 0.24m_0$ is the electron polaronic effective mass³¹ (see Supporting Information, section S3); (2) phonon spectral weight, proportional to $\omega_{\rm pk}^2$, is a measure of the change in phonon oscillator strength induced by photoexcitation.

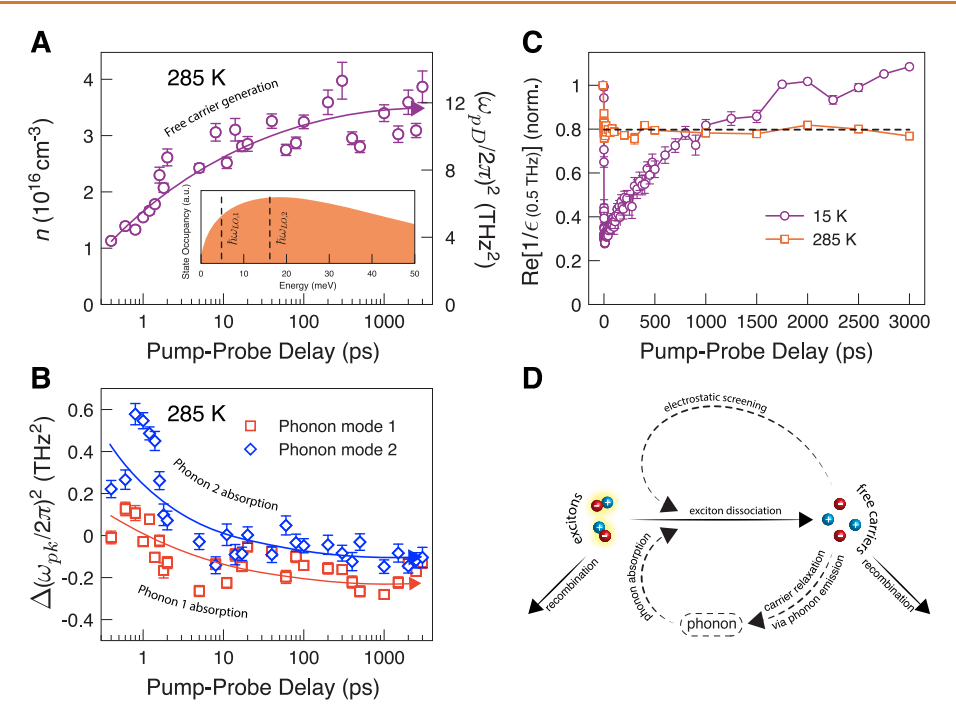


Figure 4. Room-temperature spectral weight evolution and photoenhanced free-carrier screening. Time-resolved spectral weight change of (A) free carriers and (B) phonon mode 1 (0.85 THz) and mode 2 (1.80 THz) at 285 K. (C) Electrostatic (or Coulomb) screening factor $Re(1/\tilde{\epsilon})$ at 0.5 THz as a function of pump-probe delay, at 15 and 285 K. Note the long-lived screening factor of 0.8 at 285 K even up to 3 ns. (D) Schematic showing the dissociation of excitons *via* the interplay with free carriers, electrostatic screening, and low-lying phonons to maintain a large and long-lived free-carrier population in the system.

First we have to distinguish between carrier thermalization, carrier cooling (or carrier relaxation), and carrier recombination. Carrier thermalization is the process whereby the initially excited carrier distribution by the laser pulse forms a thermal (Fermi-Dirac) distribution and is not studied here but is dominated by electron-electron interactions, and thus no energy is exchanged with the lattice. Carrier cooling is the process of electrons (holes) cascading down (up) the conduction (valence) band minimum (maximum) that involves an exchange of energy (~meV) with the lattice through phonons. Neither carrier thermalization nor carrier cooling changes the number of photogenerated electron-hole pairs, but their transport properties are modified. However, there is also an interaction among free charge carriers, phonons, and excitons. The formation of excitons through phonon emission (by free carriers) will decrease the free charge carrier population. Conversely, the dissociation of excitons via phonon absorption will increase the free charge carrier population. Finally, carrier recombination results in recombination of electron and holes and releases energy on the order of the band gap (~ eV). Carrier recombination can occur through radiative processes where the energy is radiated back to the environment or nonradiative recombination where the energy is exchanged with the lattice. A very general description of carrier recombination obeys the rate equation

$$\frac{dn(\tau)}{d\tau} = -k_1 n - k_2 n^2 - k_3 n^3$$

where the rate constants k_1 , k_2 , and k_3 describe (first-order) trap-state-mediated (second-order) bimolecular, and (third-order) trimolecular recombinations, respectively.

Figure 3A shows that, at 15 K, $1/n^2$ is linear from 10 to 600 ps, indicating that, at these carrier densities, carrier

recombination is predominantly third-order. The third-order process is usually assigned to an Auger recombination mechanism, where the energy required to recombine an electron-hole pair is provided by an intraband transition of a third charge carrier. A similar third-order recombination is also seen in MAPbI₃ with similar carrier density at the same temperature.⁶ Figure 3B shows how ω_{pD}^2 (and photogenerated carrier density n) changes with pump—probe delay time τ . The fitting parameters, obtained from the weighted-least-squares linear fit in Figure 3A from 10 to 600 ps, were used to plot the solid line in Figure 3B and then extrapolated down to 0.6 ps and up to 3000 ps. We find that the third-order recombination (solid black trace) significantly underestimates the carrier density for delay times less than 10 ps, which interestingly was previously marked as the boundary between regions ii and iii in Figure 2D. As will be explained in the subsequent paragraphs, this underestimation is primarily caused by the processes of phonon-assisted exciton dissociation and formation that affects carrier density prior to 10 ps.

We now examine the correlation between the carrier and phonon dynamics below 10 ps. To isolate the change in carrier density due only to phonon absorption/emission, we subtract the raw data in Figure 3B by the third-order recombination solid line, yielding the purple trace. Figure 3C displays the time evolution of the spectral weights of phonon modes 1 and 2. By comparing Figure 3B,C, we see that, in region ii, there is an anticorrelation between the carrier and phonon spectral weights—a decrease in phonon spectral weights (of both modes 1 and 2) is accompanied by an increase in the carrier spectral weight. The phonon dynamics in Figure 3C agree with our proposed relaxation scheme in Figure 2A, where no emission of high-energy $\hbar\omega_{\rm LO,2}$ phonons is allowed in region ii.

In the transition region between *i* and *ii*, as mentioned earlier, the high-energy tail in the finite-energy Fermi-Dirac

distribution implies a finite fraction of electrons with energies exceeding $\hbar\omega_{\text{LO},2}$, which after relaxation results in the emission of the higher-energy $\hbar\omega_{\text{LO},2}$ phonons. Hence, in this transition region, we see an increase in the spectral weight of phonon mode 2, as shown in Figure 3C. Similarly, in the transition region between ii and iii, carriers do not have enough energy to emit the $\hbar\omega_{\text{LO},2}$ phonons, and so there is only a very slow $\hbar\omega_{\text{LO},2}$ absorption all the way through region iii (see long arrow in Figure 3C). A slow emission of $\hbar\omega_{\text{LO},1}$ phonons (by free carriers) can still take place (due to high-energy tail in the state occupancy above $\hbar\omega_{\text{LO},1}$, shown in the inset of Figure 3B), resulting in the formation of excitons.

The anticorrelation between the carrier and phonon spectral weights, seen in Figure 3B,C, can be explained by the phononassisted exciton dissociation/formation. In the lead halide perovskites, the exciton binding energies are reported to be \sim 10–16 meV^{33,34} and are in the same range as the LO phonon mode energies. The excitons dissociate by absorbing LO phonons, creating unbound (i.e., free) electrons and holes, resulting in an increase in carrier spectral weight and hence carrier density. These LO phonons were provided by the relaxation of the photogenerated carriers as they relax toward the band edge (discussed in the previous section). As we pump the sample very close to the band gap, optical excitation should provide just enough energy to create excitons, leading to the coupled dynamics among carriers, phonons, and excitons via exciton-phonon coupling that was previously observed in 2D hybrid perovskites via temperature-dependent photoluminescence line width broadening.3

Figure 3D shows the coupled dynamics of carriers, excitons and phonons, with associated excitation spectrum of electron—hole pairs. Without excitons, phonon emission/absorption changes only the carrier energy, not density (red box). For the phonons to change the carrier density, they must be either absorbed by the excitons (causing exciton dissociation and increasing carrier density) or emitted by free carriers (causing exciton formation and decreasing carrier density) (see blue box).

We next wish to see if the anticorrelation between the carrier and phonon spectra weights, observed at 15 K, is still preserved at room temperature. Figure 4A shows the same anticorrelation occurring at 285 K but now over a much longer time scale—the carrier spectral weight shows a slow but monotonic increase even up to 3 ns, with a concomitant slow and monotonic decrease in the phonon spectral weights (Figure 4B) over the same time scale. Our room-temperature result is consistent with frequency-integrated TRTS data on FCPIB (see Supporting Information Figure S6), as well as those from pure FAPbI₃ under a 760 or 800 nm pump,³⁶ where the signal also shows a slow increase over the same time scale and similarly attributed to exciton dissociation. Note that the frequency-integrated TRTS signal consists of contributions from the carriers (via the DS term) and the phonons (via the PS term), which partially cancels each other. Thus, the increase in the frequency-integrated signal with pump-probe time delay in ref 36 is not as large as that shown in Figure 4A, which contains the carrier part only. It is fascinating that, even up to 3 ns, the free-carrier density is still increasing and shows no sign

Pump-Enhanced Free-Carrier Screening. We now turn to another effect of carrier—phonon coupling on the photogenerated carriers, namely, electrostatic screening of electron—hole pairs. The screening cloud surrounding the

charge carriers efficiently renormalizes the bare Coulomb potential $V_{\rm bare}$ via the dielectric function $\tilde{\epsilon}(\omega,\tau)$. The effective screened potential $V_{\rm eff}$ can be expressed as

$$V_{\mathrm{eff}}(\omega, \, au) = rac{V_{\mathrm{bare}}}{\widetilde{\epsilon}(\omega, \, au)}$$

Figure 4C shows, at 15 and 285 K, the photoinduced enhancement of free-carrier screening factor $\mathrm{Re}(1/\tilde{\epsilon})$ at 0.5 THz, at different pump—probe time delays, normalized to the value before photoexcitation. At 15 K, though the screening is stronger at short time delays, it quickly recovers toward the equilibrium value, whereas at 285 K, the screening factor remains at a constant value of 80% (of the equilibrium value) up to 3 ns. The presence of screening reduces the exciton binding energy⁵ and thus further enhances exciton dissociation to free electrons and holes. Together with the results of the previous section, at room temperature, both electrostatic screening and exciton dissociation can now compete with carrier recombination, thus slowing down the decrease of carriers due to recombination and therefore maintaining a large free-carrier population over a long period of time.

A recent time-resolved photoluminescence and elastic neutron scattering study revealed a possible source of this screening in FAPbI $_3$ —the rotation of the organic cation $HC(NH_2)_2^+$ molecules in response to the presence of photogenerated charge carriers maximizes screening, resulting in a carrier lifetime longer than that in MAPbI $_3$.

Figure 4D summarizes the interplay among free carriers, excitons, and low-lying phonon modes, based on our present work. Upon photoexcitation with a near-band-gap-energy photon, both free carriers and excitons are generated. Thermal energy provides these carriers with sufficient kinetic energy. Subsequently, a large number of hot phonons is generated via carrier cooling. These hot phonons can be reabsorbed by excitons, thus dissociating the excitons to form free charge carriers. At the same time, Coulomb screening is enhanced due to the presence of photogenerated free charge carriers—this photoenhanced Coulomb screening results in a reduction of the exciton binding energy, which further facilitates the dissociation of excitons and creates even more free charge carriers. This combination of phonon-assisted exciton dissociation, carrier regeneration, and enhanced carrier screening results in a positive feedback that ensures a long-lived free charge carrier population. This favorable circumstance is even more pronounced at room temperature—the large thermal energy of the carriers above the LO phonon mode energies (see inset of Figure 4A) ensures more carrier relaxation channels and phonon emission (by carriers). This in turn causes a long-lived (~ns) phonon absorption process by excitons (Figure 4B), resulting in enhanced exciton dissociation and therefore large carrier density (Figure 4A). However, the low-energy phonon modes provide more scattering channels for the free charge carriers, reducing their carrier mobility, compared to systems with higher energy phonon modes (e.g., GaAs³⁰). Note that the strong photoinduced change in the phonon modes and long rise in carrier population were only observed with an excitation at the band edge energy in FA-based perovskite family. They were not seen in non-FA-based perovskites nor when the pump excitation energy is not at the gap edge. 6,36

In our picture, the LO phonons act as mediators between the free carriers and excitons, where phonon emission by carriers forms excitons, whereas phonon absorption by excitons

forms free carriers. For this to happen, the LO phonon energy must be similar to the binding energy of the excitons (which is true for the halide perovskite family), and these phonons must remain in the system for emission and reabsorption to continually take place. An alternative way of explaining this "oscillation" between the carrier and exciton densities is a coherent quantum superposition between the excitonic states and free carriers, neither of which are now an eigenstate due to coupling with phonons.

A previous transient absorption work²¹ observed a very slow carrier cooling and attributed it to the presence of a hot phonon bottleneck upon photoexcitation with higher energy photons. Subsequent works attribute the observed hot phonon bottleneck to (1) the suppression of the Klemens relaxation pathway in MAPbI₃²² or (2) acoustic-optical phonon upconversion that is especially strong in FAPbI3 compared to MAPbI₃,³⁹ due to the overlapping phonon branches caused by the presence of the organic cations. Hence, we can assume that the decay of optical to acoustic phonons is very weak, resulting in a long-lived optical (i.e., hot) phonon population. In our present work, due to the ability of TRTS to directly track the carrier density and phonon spectral weights, we found that the hot phonons contribute not only to slower carrier cooling but also to carrier generation via phonon-assisted exciton dissociation.

CONCLUSION

In summary, one of the distinguishing features of the Pb halide semiconductor system is the presence of low-frequency phonon modes. These low-frequency modes reduce the carrier mobility via the introduction of more scattering pathways (emission and absorption) relative to semiconductors with higher-frequency modes, where only phonon emission is likely. There is a large population of phonons at room temperature (thus the "liquid-like" nature of the system) that can help to reduce carrier trapping into shallow defects. It is also apparently easier to drive the phonon system out-ofequilibrium, leading to slower carrier cooling. Here, we show that time-resolved THz spectroscopy is ideally suited for studying electron-phonon interactions in the Pb halide semiconductor system. TRTS can monitor both the carrier population as well as the low-frequency phonon modes immediately after photoexcitation and thus is able to infer the interplay between the carrier, phononic, and excitonic degrees of freedom. We show that, as expected, for a good semiconductor that the carriers and excitons relax via carrierphonon interactions (phonon emission and absorption) establishing a thermal equilibrium between phonons, carriers, and excitons. On one hand, excitons dissociate via phonon absorption to yield free carriers. On the other hand, excitons can form via phonon emission from free carriers, thus reducing the free-carrier population. Our analysis directly resolves these interactions on the picosecond time scale.

METHODS

Sample Fabrication. Formamidinium iodide (FAI) was synthesized according to ref 12. The reagents were dissolved in ethanol and recrystallized at -3 °C overnight. Perovskite precursor solution FA_{0.85}Cs_{0.15}Pb(I_{0.97}Br_{0.03})₃ was prepared by dissolving FAI, CsI, PbI₂, and PbBr₂ with respective stoichiometric ratio in DMF/DMSO (4:1 v/v) at 80 °C. The *z*-cut quartz substrates (10 mm \times 10 mm \times 1 mm) were cleaned thoroughly in Hellmanex II solution (1% v/v), deionized water, acetone, and isopropyl alcohol for 15 min each in an

ultrasonic bath. Immediately before deposition of the photovoltaic precursor solution, the substrates were subjected to an air plasma treatment for 5 min and subsequently transferred to a nitrogen glovebox. The perovskite solution (1 mol/L) was spin-coated on z-cut quartz at 1000 rpm for 10 s and 4000 rpm for 30 s. Two hundred fifty microliters of chlorobenzene was dripped on the sample surface at 15 s of the second step spin-coating. Subsequently, the perovskite layer was annealed at 80 $^{\circ}\mathrm{C}$ for 5 min, 120 $^{\circ}\mathrm{C}$ for 5 min, and 180 $^{\circ}\mathrm{C}$ for 30 min. The thickness of our final polycrystalline FCPIB film was 580 \pm 20 nm. The sample was mounted in a cryostat with a cryocooler for cooling to 15 K.

Time-Resolved Terahertz Spectroscopy. The sample was excited by 790 \pm 10 nm (1.57 \pm 0.02 eV) optical pump pulses from a band-pass-limited output of an optical parametric amplifier set at 790 nm. The pump-probe time delay, τ , between the near-infrared pump pulse and the terahertz (THz) pulse, and the THz time delay, t, between the THz pulse and the gate pulse, are set by two motorized delays stages. THz pulses (with frequency range 0.5 to 2.3 THz) are generated in a 1 mm thick ZnTe crystal through optical rectification, transmitted through the thin film, and detected by electro-optical sampling in another ZnTe crystal. By modulating both the pump and probe beams, both the transmitted THz electric field $E(t,\tau)$ and its photoinduced change $\Delta E(t,\tau)$ are measured simultaneously at different pump-probe time delays τ (see Figure 1A). At each pump-probe time delay τ , we scan the THz emitter delay in reverse, with pump and gate delays fixed. This synchronization procedure ensures that every part of the measured THz pulse experiences the same time delay from the pump pulse³⁰ and enables sub-THzwavelength detection. In this case, the time resolution of TRTS is only limited by the laser pulse duration in THz detection crystal $(\sim 100 \text{ fs})$ rather than the THz pulse duration itself. For more details, one can refer to the work by Beard et al.³⁰ By use of an analytical expression of the transmission function of a film on a substrate without using any thin-film approximation, we extract the photoinduced change in the complex optical conductivity (or photoconductivity) $\Delta \tilde{\sigma}(\omega,\tau)$. The photoconductivity contains both real $\Delta\sigma_1$ and imaginary $\Delta\sigma_2$ parts without requiring the use of the Kramers-Kronig transformation.

ASSOCIATED CONTENT

S Supporting Information

The Supporting Information is available free of charge on the ACS Publications website at DOI: 10.1021/acsnano.9b02049.

Dielectric function and loss function analysis; LO phonon mode consistency with the Cochran–Cowley relation; carrier–phonon coupling constant calculation; *J–V* characteristics; scanning electron microscopy images of FCPIB thin films; temperature-dependent absorption spectra; room-temperature photoluminescence; phonon anharmonicity; frequency-integrated TRTS; combined photoconductivity model from phonon and carriers; and temperature-dependent THz conductivities of thin-film FCPIB (PDF)

AUTHOR INFORMATION

Corresponding Authors

*E-mail: chan.laovorakiat@gmail.com. *E-mail: matt.beard@nrel.gov. *E-mail: elbertchia@ntu.edu.sg.

ORCID ®

Yeng Ming Lam: 0000-0001-9390-8074 Jian-Xin Zhu: 0000-0001-7991-3918 Matthew C. Beard: 0000-0002-2711-1355 Elbert E. M. Chia: 0000-0003-2066-0834

Notes

The authors declare no competing financial interest.

ACKNOWLEDGMENTS

E.E.M.C. acknowledges support from the Singapore Ministry of Education AcRF Tier 2 (MOE2015-T2-2-065 and MOE2016-T2-1-054). C.L. is grateful for the support from the Theoretical and Computational Science (TaCS) Center, Thailand Research Fund (MRG6080264), and KMUTT 55th Anniversary Commemorative Fund. M.C.B. acknowledges funding from the Center for Hybrid Organic Inorganic Semiconductors for Energy (CHOISE) an Energy Frontier Research Center funded by the Office of Science of the U.S. Department of Energy. Part of this work was authored in part by Alliance for Sustainable Energy, LLC, the manager and operator of the National Renewable Energy Laboratory for the U.S. Department of Eenrgy (ODE) under Contract No. DE-AC36-08GO28308. Y.M.L. acknowledges financial support from a Ministry of Education, Singapore, Tier 1 Funding (RG105/18). R.A.M. thanks the ONR and ARO for their support. M.-E.M.-B. is grateful to the Nanyang Technological University for supporting the Biophysics Center. The work was supported in part by the Center for Integrated Nanotechnologies, a U.S. DOE BES user facility.

REFERENCES

- (1) Snaith, H. J. Perovskites: The Emergence of a New Era for Low-Cost, High-Efficiency Solar Cells. *J. Phys. Chem. Lett.* **2013**, *4*, 3623–3630.
- (2) Yin, W.-J.; Shi, T.; Yan, Y. Unique Properties of Halide Perovskites as Possible Origins of the Superior Solar Cell Performance. *Adv. Mater.* **2014**, *26*, 4653–4658.
- (3) Stranks, S. D.; Eperon, G. E.; Grancini, G.; Menelaou, C.; Alcocer, M. J. P.; Leijtens, T.; Herz, L. M.; Petrozza, A.; Snaith, H. J. Electron—Hole Diffusion Lengths Exceeding 1 Micrometer in an Organometal Trihalide Perovskite Absorber. *Science* **2013**, 342, 341—344.
- (4) Xing, G.; Mathews, N.; Sun, S.; Lim, S. S.; Lam, Y. M.; Grätzel, M.; Mhaisalkar, S.; Sum, T. C. Long-Range Balanced Electron- and Hole-Transport Lengths in Organic-Inorganic CH₃NH₃PbI₃. *Science* **2013**, 342, 344–347.
- (5) Manser, J. S.; Kamat, P. V. Band Filling with Free Charge Carriers in Organometal Halide Perovskites. *Nat. Photonics* **2014**, *8*, 737–743.
- (6) La-o-vorakiat, C.; Salim, T.; Kadro, J.; Khuc, M. T.; Haselsberger, R.; Cheng, L.; Xia, H.; Gurzadyan, G. G.; Su, H.; Lam, Y. M.; Marcus, R. A.; Michel-Beyerle, M.-E.; Chia, E. E. M. Elucidating the Role of Disorder and Free-Carrier Recombination Kinetics in CH₃NH₃PbI₃ Perovskite Films. *Nat. Commun.* **2015**, *6*, 7903.
- (7) Wu, X.; Tan, L. Z.; Shen, X.; Hu, T.; Miyata, K.; Trinh, M. T.; Li, R.; Coffee, R.; Liu, S.; Egger, D. A.; Makasyuk, I.; Zheng, Q.; Fry, A.; Robinson, J. S.; Smith, M. D.; Guzelturk, B.; Karunadasa, H. I.; Wang, X.; Zhu, X.; Kronik, L.; et al. Light-Induced Picosecond Rotational Disordering of the Inorganic Sublattice in Hybrid Perovskites. Sci. Adv. 2017, 3, e1602388.
- (8) Noh, J. H.; Im, S. H.; Heo, J. H.; Mandal, T. N.; Seok, S. I. Chemical Management for Colorful, Efficient, and Stable Inorganic—Organic Hybrid Nanostructured Solar Cells. *Nano Lett.* **2013**, *13*, 1764–1769.
- (9) Yang, J.; Siempelkamp, B. D.; Liu, D.; Kelly, T. L. Investigation of CH₃NH₃PbI₃ Degradation Rates and Mechanisms in Controlled Humidity Environments Using *In Situ* Techniques. *ACS Nano* **2015**, 9, 1955–1963.
- (10) Lee, J.-W.; Kim, D.-H.; Kim, H.-S.; Seo, S.-W.; Cho, S. M.; Park, N.-G. Formamidinium and Cesium Hybridization for Photo-

and Moisture-Stable Perovskite Solar Cell. Adv. Energy Mater. 2015, 5, 1501310.

- (11) Kulbak, M.; Gupta, S.; Kedem, N.; Levine, I.; Bendikov, T.; Hodes, G.; Cahen, D. Cesium Enhances Long-Term Stability of Lead Bromide Perovskite-Based Solar Cells. *J. Phys. Chem. Lett.* **2016**, 7, 167–172.
- (12) Eperon, G. E.; Stranks, S. D.; Menelaou, C.; Johnston, M. B.; Herz, L. M.; Snaith, H. J. Formamidinium Lead Trihalide: A Broadly Tunable Perovskite for Efficient Planar Heterojunction Solar Cells. *Energy Environ. Sci.* **2014**, *7*, 982–988.
- (13) Yang, W. S.; Park, B.-W.; Jung, E. H.; Jeon, N. J.; Kim, Y. C.; Lee, D. U.; Shin, S. S.; Seo, J.; Kim, E. K.; Noh, J. H.; et al. Iodide Management in Formamidinium-Lead-Halide—Based Perovskite Layers for Efficient Solar Cells. *Science* **2017**, *356*, 1376—1379.
- (14) Ulbricht, R.; Hendry, E.; Shan, J.; Heinz, T. F.; Bonn, M. Carrier Dynamics in Semiconductors Studied with Time-Resolved Terahertz Spectroscopy. *Rev. Mod. Phys.* **2011**, *83*, 543–586.
- (15) Ahmed, T.; La-o-vorakiat, C.; Salim, T.; Lam, Y. M.; Chia, E. E. M.; Zhu, J.-X. Optical Properties of Organometallic Perovskite: An *Ab Initio* Study Using Relativistic GW Correction and Bethe-Salpeter Equation. *Europhys. Lett.* **2014**, *108*, *67015*.
- (16) La-o-vorakiat, C.; Xia, H.; Kadro, J.; Salim, T.; Zhao, D.; Ahmed, T.; Lam, Y. M.; Zhu, J.-X.; Marcus, R. A.; Michel-Beyerle, M.-E.; Chia, E. E. M. Phonon Mode Transformation Across the Orthohombic—Tetragonal Phase Transition in a Lead Iodide Perovskite CH₃NH₃PbI₃: A Terahertz Time-Domain Spectroscopy Approach. *J. Phys. Chem. Lett.* **2016**, *7*, 1–6.
- (17) Zhao, D.; Skelton, J. M.; Hu, H.; La-o-vorakiat, C.; Zhu, J.-X.; Marcus, R. A.; Michel-Beyerle, M.-E.; Lam, Y. M.; Walsh, A.; Chia, E. E. M. Low-Frequency Optical Phonon Modes and Carrier Mobility in the Halide Perovskite CH₃NH₃PbBr₃ Using Terahertz Time-Domain Spectroscopy. *Appl. Phys. Lett.* **2017**, *111*, 201903.
- (18) La-o-vorakiat, C.; Cheng, L.; Salim, T.; Marcus, R. A.; Michel-Beyerle, M.-E.; Lam, Y. M.; Chia, E. E. M. Phonon Features in Terahertz Photoconductivity Spectra Due to Data Analysis Artifact: A Case Study on Organometallic Halide Perovskites. *Appl. Phys. Lett.* **2017**, *110*, 123901.
- (19) Wehrenfennig, C.; Liu, M.; Snaith, H. J.; Johnston, M. B.; Herz, L. M. Charge-Carrier Dynamics in Vapour-Deposited Films of the Organolead Halide Perovskite CH₃NH₃PbI_{3-x}Cl_x. *Energy Environ. Sci.* **2014**, *7*, 2269–2275.
- (20) Yettapu, G. R.; Talukdar, D.; Sarkar, S.; Swarnkar, A.; Nag, A.; Ghosh, P.; Mandal, P. Terahertz Conductivity within Colloidal CsPbBr₃ Perovskite Nanocrystals: Remarkably High Carrier Mobilities and Large Diffusion Lengths. *Nano Lett.* **2016**, *16*, 4838–4848.
- (21) Yang, Y.; Ostrowski, D. P.; France, R. M.; Zhu, K.; van de Lagemaat, J.; Luther, J. M.; Beard, M. C. Observation of a Hot-Phonon Bottleneck in Lead-Iodide Perovskites. *Nat. Photonics* **2016**, *10*, 53–59.
- (22) Fu, J.; Xu, Q.; Han, G.; Wu, B.; Huan, C. H. A.; Leek, M. L.; Sum, T. C. Hot Carrier Cooling Mechanisms in Halide Perovskites. *Nat. Commun.* **2017**, *8*, 1300.
- (23) Wright, A. D.; Verdi, C.; Milot, R. L.; Eperon, G. E.; Pérez-Osorio, M. A.; Snaith, H. J.; Giustino, F.; Johnston, M. B.; Herz, L. M. Electron—Phonon Coupling in Hybrid Lead Halide Perovskites. *Nat. Commun.* **2016**, *7*, 11755.
- (24) Lloyd-Hughes, J.; Jeon, T.-I. A Review of the Terahertz Conductivity of Bulk and Nano-Materials. *J. Infrared, Millimeter, Terahertz Waves* **2012**, 33, 871–925.
- (25) Lowndes, R. P. Influence of Lattice Anharmonicity on the Longitudinal Optic Modes of Cubic Ionic Solids. *Phys. Rev. B* **1970**, *1*, 2754–2763.
- (26) Huber, R.; Kübler, C.; Tübel, S.; Leitenstorfer, A.; Vu, Q. T.; Haug, H.; Köhler, F.; Amann, M.-C. Femtosecond Formation of Coupled Phonon-Plasmon Modes in InP: Ultrabroadband THz Experiment and Quantum Kinetic Theory. *Phys. Rev. Lett.* **2005**, *94*, 027401.

(27) Smith, N. V. Classical Generalization of the Drude Formula for the Optical Conductivity. *Phys. Rev. B: Condens. Matter Mater. Phys.* **2001**, *64*, 155106.

- (28) Cocker, T. L.; Baillie, D.; Buruma, M.; Titova, L. V.; Sydora, R. D.; Marsiglio, F.; Hegmann, F. A. Microscopic Origin of the Drude-Smith Model. *Phys. Rev. B: Condens. Matter Mater. Phys.* **2017**, *96*, 205439.
- (29) Whalley, L. D.; Skelton, J. M.; Frost, J. M.; Walsh, A. Phonon Anharmonicity, Lifetimes, and Thermal Transport in CH₃NH₃PbI₃ from Many-Body Perturbation Theory. *Phys. Rev. B: Condens. Matter Mater. Phys.* **2016**, 94, 220301.
- (30) Beard, M. C.; Turner, G. M.; Schmuttenmaer, C. A. Transient Photoconductivity in GaAs as Measured by Time-Resolved Terahertz Spectroscopy. *Phys. Rev. B: Condens. Matter Mater. Phys.* **2000**, *62*, 15764–15777.
- (31) Amat, A.; Mosconi, E.; Ronca, E.; Quarti, C.; Umari, P.; Nazeeruddin, M. K.; Grätzel, M.; De Angelis, F. Cation-Induced Band-Gap Tuning in Organohalide Perovskites: Interplay of Spin—Orbit Coupling and Octahedra Tilting. *Nano Lett.* **2014**, *14*, 3608—3616
- (32) Kasap, S., Capper, P., Eds. Springer Handbook of Electronic and Photonic Materials; Springer: New York, 2017.
- (33) Galkowski, K.; Mitioglu, A.; Miyata, A.; Plochocka, P.; Portugall, O.; Eperon, G. E.; Wang, J. T.-W.; Stergiopoulos, T.; Stranks, S. D.; Snaith, H. J.; et al. Determination of the Exciton Binding Energy and Effective Masses for Methylammonium and Formamidinium Lead Tri-Halide Perovskite Semiconductors. *Energy Environ. Sci.* **2016**, *9*, 962–970.
- (34) Luo, L.; Men, L.; Liu, Z.; Mudryk, Y.; Zhao, X.; Yao, Y.; Park, J. M.; Shinar, R.; Shinar, J.; Ho, K.-M.; Perakis, I. E.; Vela, J.; Wang, J. Ultrafast Terahertz Snapshots of Excitonic Rydberg States and Electronic Coherence in an Organometal Halide Perovskite. *Nat. Commun.* 2017, *8*, 15565.
- (35) Ni, L.; Huynh, U.; Cheminal, A.; Thomas, T. H.; Shivanna, R.; Hinrichsen, T. F.; Ahmad, S.; Sadhanala, A.; Rao, A. Real-Time Observation of Exciton—Phonon Coupling Dynamics in Self-Assembled Hybrid Perovskite Quantum Wells. *ACS Nano* **2017**, *11*, 10834—10843.
- (36) Piatkowski, P.; Cohen, B.; Ponseca, C. S., Jr; Salado, M.; Kazim, S.; Ahmad, S.; Sundström, V.; Douhal, A. Unraveling Charge Carriers Generation, Diffusion, and Recombination in Formamidinium Lead Triiodide Perovskite Polycrystalline Thin Film. *J. Phys. Chem. Lett.* **2016**, *7*, 204–210.
- (37) Huber, R.; Tauser, F.; Brodschelm, A.; Bichler, M.; Abstreiter, G.; Leitenstorfer, A. How Many-Particle Interactions Develop after Ultrafast Excitation of an Electron—Hole Plasma. *Nature* **2001**, *414*, 286–289.
- (38) Chen, T.; Chen, W.-L.; Foley, B. J.; Lee, J.; Ruff, J. P. C.; Ko, J. Y. P.; Brown, C. M.; Harriger, L. W.; Zhang, D.; Park, C.; Yoon, M.; Chang, Y.-M.; Choi, J. J.; Lee, S.-H. Origin of Long Lifetime of Band-Edge Charge Carriers in Organic—Inorganic Lead Iodide Perovskites. *Proc. Natl. Acad. Sci. U. S. A.* 2017, 114, 7519—7524.
- (39) Yang, J.; Wen, X.; Xia, H.; Sheng, R.; Ma, Q.; Kim, J.; Tapping, P.; Harada, T.; Kee, T. W.; Huang, F.; et al. Acoustic-Optical Phonon Up-Conversion and Hot-Phonon Bottleneck in Lead-Halide Perovskites. *Nat. Commun.* **2017**, *8*, 14120.